# Defect-enhanced $CO_2$ Reduction Catalytic Performance in O-terminated MXenes

*Hetian Chen,‡[1] Dr. Albertus D. Handoko,‡[2] Tianshuai Wang,[1] Jiale Qu,[1] Jiewen Xiao,[1] Xiaopeng Liu,[1] Prof. Dominik Legut,[3] Prof. Zhi Wei Seh,*[,2] and Prof. Qianfan Zhang*[,1]*

*1 School of Materials Science and Engineering, Beihang University, Beijing, 100191, P. R. China.*

*2 Institute of Materials Research and Engineering, Agency for Science, Technology and Research (A*STAR), 2 Fusionopolis Way, Innovis, Singapore 138634, Singapore.*

*3 IT4Innovations, VSB-Technical University of Ostrava, 17. listopadu 2172/15, CZ-708 00 Ostrava, Czech Republic.*

*E-mail: qianfan@buaa.edu.cn, sehzw@imre.a-star.edu.sg*

*† Electronic supplementary information (ESI) available*

*‡ These authors contributed equally to this work*

## Abstract

Electrochemical carbon dioxide reduction reaction ($CO_2$RR) represents a promising way to generate fuels and chemical feedstock sustainably. Recently, studies have shown that two-dimensional metal carbides and nitrides (MXenes) can be promising $CO_2$RR electrocatalysts, due to the alternating –C and –H coordination with intermediates that decouples scaling relations seen on transition metal catalysts. However, further tuning of MXenes' electronic and surface structure is still possible to reach higher turnover and selectivity. To this end, defect engineering of MXenes for electrochemical $CO_2$RR has not been investigated to date. In this work, first-principles modelling simulation is employed to systematically investigate $CO_2$RR on $M_2XO_2$ type MXenes with transition metal and carbon/nitrogen

vacancies. We found that the –C coordinated intermediates take the form of fragments (*e.g.* *COOH, *CHO) while the –H coordinated intermediates form a complete molecule (*e.g.* *HCOOH, *$H_2CO$). Interestingly, the fragment-type intermediates become more strongly bound when transition metal vacancy is present on most MXenes, while the molecule-type intermediates are largely unaffected, allowing the $CO_2$RR overpotential to be tuned. The most promising defective MXene is $Hf_2NO_2$ containing Hf vacancies, with a low overpotential of 0.45 V. More importantly, through electronic structure analysis, we observed that the MXene's Fermi level changes significantly with the presence of vacancies, indicating that the Fermi level shift can be used as an ideal descriptor to rapidly predict the catalytic performance of defective MXenes. We show that such an evaluation strategy is applicable to other catalysts beyond MXenes, thereby enhancing high throughput screening efforts for accelerated catalyst discovery.

# Introduction

Electrocatalytic $CO_2$ reduction reaction ($CO_2$RR) plays a vital role in obtaining renewable fuels and chemical raw materials from $CO_2$ and $H_2O$ under ambient conditions using clean energy sources.[1] However, improvement of the intrinsic activity of $CO_2$RR catalysts remains a major challenge due to competing hydrogen evolution reaction (HER) and unfavourable scaling relationship of similarly bound intermediates.[2] Copper-based materials are the most promising and studied $CO_2$RR catalysts due to their ability to convert $CO_2$ to a diverse array of hydrocarbons and alcohols.[3] Despite intensive experimental and theoretical research, the performance of existing catalysts is still far from satisfactory.[4]

Recently, a relatively new family of two-dimensional (2D) transition metal carbides and nitrides (collectively referred to as MXenes) have attracted extensive research attention due to their unusual electronic, mechanical and optical properties,[5] with the chemical formula $M_{n+1}X_nT_x$ ($n$ = 1-4; M = early transition metal; X = C and/or N; $T_x$ = surface terminations). Previous works have predicted that MXenes can be one of the most promising 2D material systems to facilitate the $CO_2$RR process.[6] A majority of theoretical studies to date assume perfect crystal models for computational simplicity.[7] However, real structures are rarely perfect. Most crystals, especially MXenes, possess defects on the surface and edges due to the invasive delamination process.[8] Further, these defects have been shown to be thermodynamically and dynamically stable by first-principle calculations.[9]

In catalysis, defect sites have been proposed to have unconventional adsorption behaviours.[10] These odd adsorption in turn leads to selective stabilisation of certain intermediates, opening new reaction pathways that are previously inaccessible in perfect structures. The different adsorption behaviour is believed to stem from localised alteration of the bulk electronic states and surface properties, i.e. modification by substrate-adsorbate interaction.[11] Specific to $CO_2$RR, a variety of defective sites in graphene have been shown to primarily affect *COOH binding, but not *CO.[11e] This results in decoupling of $\Delta G_{COOH}$ and $\Delta G_{CO}$, despite both of these intermediates being coordinated to the defective graphene substrate through –C. The stronger *COOH binding would translate to a more efficient $CO_2$RR on defective graphene-like structure, which is shown experimentally on nitrogen-doped CNTs[12] or N-doped graphene foams.[13]

Decoupling of linear scaling relationship between intermediates can arise from nanostructuring.[14] Nanoscopic catalysts provide diverse adsorption sites with low coordination number that show dissimilar adsorption configuration and strength.[15] For example, $CO_2$RR on Cu “single-atom” and

nanosheet catalysts were reported to have more inclination to produce CO and $CH_4$,[16] a marked departure from the multi-carbon products commonly displayed on bulk Cu.[3, 16] However, these nanocatalysts are difficult to produce in large scale and prone to rapid deactivation due to aggregation.[17]

However, MXenes provide a different strategy to decouple linear scaling relationship. Although MXenes' band structure around the Fermi level is dominated by the d-orbitals of the M atoms,[18] some states contain hybridised M-X or M-$T_x$ states.[19] Therefore, with variations in either M, X or $T_x$ components, different interactions with $CO_2$RR intermediates can be expected. Indeed, (perfect) MXenes have been calculated to have atypical intermediates for $CO_2$RR to $CH_4$, involving both –H and –C coordinated intermediates.[6b-d] However, we note that systematic studies on more realistic, defective MXenes structures for $CO_2$RR are absent.

As-synthesized MXene powders have been shown to contain mixed $T_x$ group of –OH, –O and –F with varying composition depending on the processing method.[20] However, more recent investigations found that –O is the most stable, as other –OH and–F tend to be converted into –O under externally applied electron or heat.[21] Thus, in the present work, we conduct a theoretical study to investigate the catalytic effect of point defects in 16 types of $M_2XO_2$ type MXenes (M = Ti, Zr, Hf, V, Nb, Ta, Mo, W, while X = C, N). $Sc_2XO_2$ and $Y_2XO_2$ are excluded as they tend to have high hydroxyl coverage and the O-terminated structure was unstable in simulation.[22] $Cr_2XO_2$ is excluded as well because *COOH adsorption was unstable when $V_X$ was introduced to the system, forming $CO_2$ and *H instead. DFT is an ideal platform to conduct a systematic and holistic look on how the defects, including $V_M$ (M atom vacancy) and $V_X$ (X atom vacancy), exert influence on catalytic performance.[23] Our results suggest that, although the presence of either $V_M$ or $V_X$ does not break the common scaling

relationship, its effect is non-uniform across different intermediates. Specifically, $V_M$ and $V_X$ exhibit a more profound influence on the fragment-type intermediates but minimal effect on the molecule-like intermediates. $V_{Hf}$-$Hf_2NO_2$ ($Hf_2NO_2$ containing Hf vacancy) is identified as the most promising catalyst among these defective MXenes, with $CO_2$RR limiting potential ($UL_{CO2}$) of -0.28 V and high $CO_2$RR selectivity against HER (all potentials in this work are referenced to the reversible hydrogen electrode, RHE). Further electronic structure analysis demonstrates that the change of Fermi level has a good linear relationship to the binding energy change of intermediates. Such increase/decrease of Fermi level energy induced by the filling of anti-bonding states can serve as an excellent descriptor for the catalytic activity. This study provides insight on fine-tuning the $CO_2$RR catalytic performance to the peak of volcano curve, and facilitates the process of obtaining low cost, environmentally friendly and high-performance catalysts.

# Results and Discussion

## Substrate structure

16 different types of O-terminated MXenes $M_2XO_2$ (M = Ti, Zr, Hf, V, Nb, Ta, Mo, W, while X = C, N) are systematically studied in the pristine, $V_M$ containing and $V_X$ containing variants. It is known from previous studies of pristine $M_2XO_2$ that different combinations of M and X can induce different stacking patterns.[6c] Consistent with the literature, the *fcc* hollow site is the most energetically favourable configuration for –O $T_x$ sites for most $M_2XO_2$ MXenes except for $Mo_2CO_2$, $W_2CO_2$, $Mo_2NO_2$, $W_2NO_2$, $Ta_2NO_2$ and $Nb_2NO_2$, where the *hcp* hollow site is preferred (Table S1).

To model the vacancies, one M atom or X atom is removed from the pristine model, and the

geometry is optimised further. The typical atomic conformations for defective MXenes containing $V_M$ and $V_X$ are shown as Figure 1(a) and (b). In the case of MXenes with $V_M$, the surrounding O-terminations are inclined to move slightly away from the vacancy. MXenes with $V_X$ also result in slightly distorted structure, but with less severe displacements compared to the $V_M$ case. The formation energies of most $V_M$ and $V_X$ cases studied here (Table S3) are comparable or more negative than those of defective graphene (about 7.4 eV[24]), indicative of their high likelihood of formation.

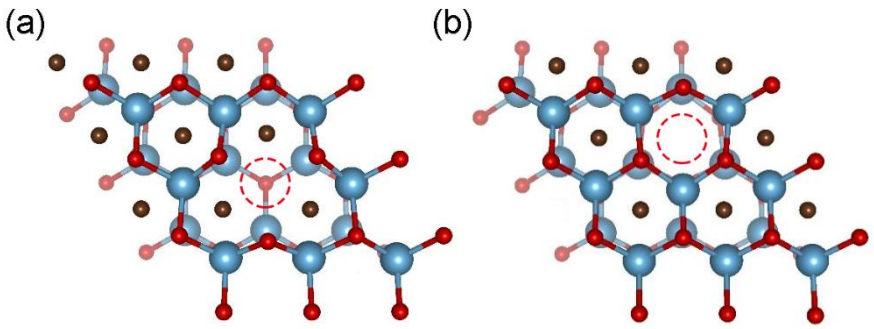


**Figure 1.** The atomic structure of $M_2XO_2$ MXene with (a) $V_M$ and (b) $V_X$ ($Mo_2CO_2$ is shown here).

## Reaction mechanism

After determining the energetically favourable adsorption conformation (Table S1), we first calculate the most favourable reaction pathway from $CO_2$ to $CH_4$ on pristine $M_2XO_2$. A free energy diagram for a pristine $Hf_2NO_2$ substrate is drawn in Figure 2a (black lines). Along this pathway, it is found that two different kinds of adsorbates with different interaction mechanisms to the substrate exists.[25] The first kind of adsorbates takes the form of molecular fragments and typically coordinated through –C, such as *COOH and *$CH_3$. These adsorbates possess unpaired electrons and typically form a strong chemical bond with the –O surface termination via orbitals rehybridisation. Such chemical bonding dominated interaction is sensitive to changes in the electronic structure, for example through Pauli

repulsion, and it is rational to predict that the adsorption geometry and adsorption strength can be profoundly affected by the presence of defects in the substrates. The second kind of adsorbates take the form of complete molecules, such as *HCOOH or *$H_2CO$. These adsorbates do not have free radicals, as every atom has filled 8 electrons through the covalent interaction with each other. Unlike the fragment-types, the complete molecule adsorbates bind to the substrate through weaker van der Waals interaction or hydrogen bond (–H coordination). As a result, the binding strength of these adsorbates are less affected by the modification of substrate electronic structure. To understand the difference between fragment- and molecule-type intermediate-substrate interaction, the deformation charge density of *COOH and *HCOOH bound on pristine $Hf_2NO_2$ MXene are plotted as Figure 2b and 2c respectively. It can be clearly seen that the charge migration of molecule-type intermediate is much smaller than that of fragment-type, indicating that the interaction between molecule and substrate is substantially weaker in the former case.

We note that the fragment-type adsorbates are formed at the odd number of proton coupled electron transfer (PCET) steps, while the molecule-type appear at the even number steps (Figure 2a). The alternating intermediates-substrate coordination presents an opportunity to tune the free energy ($\Delta G$) of adjacent steps differently by introducing defects that can alter MXene's band structure. To investigate this, the free energy profiles for $CO_2RR$ to $CH_4$ on pristine $M_2XO_2$ MXenes and their defective variants containing $V_M$ and $V_X$ are systematically computed (Figure 2a and S2).

A comparison of the free energy diagrams for pristine and defective $M_2XO_2$ structures reveals that the addition of $V_M$ or $V_X$ radically changes the reaction energies of odd PCET steps, while keeping the even PCET steps similar to the pristine structure. More specifically, the presence of $V_M$ appears to strengthen the chemical bond between the fragment-type intermediate and the substrate while the $V_X$

will weaken the bond. However, this would mean that the potential limiting steps of a $M_2XO_2$ MXene can be tuned by controlling the type of vacancies it has. Generally, the potential limiting steps that occur during the even to odd transition can be made less negative by the presence of $V_M$, while $V_X$ will make them more negative. The inverse is true if the potential limiting steps take place from odd to even transition.

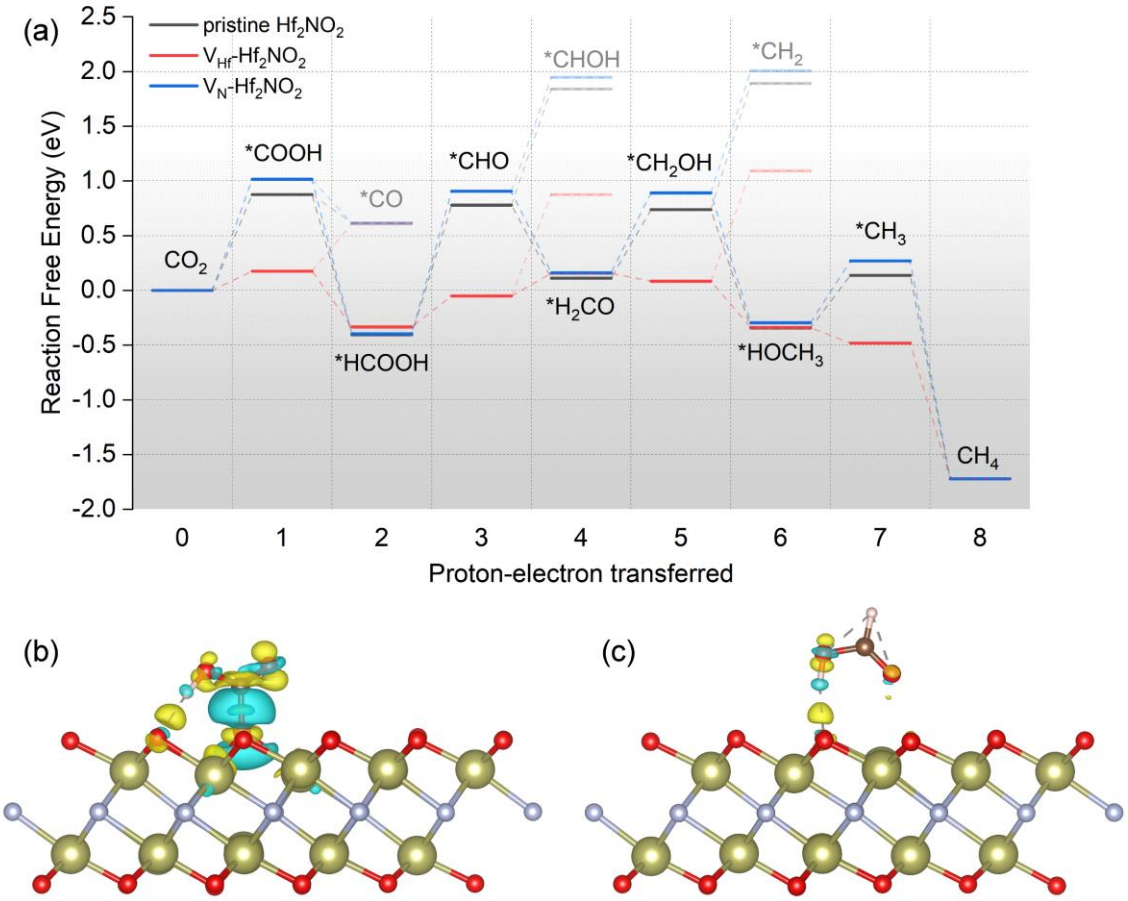


**Figure 2.** (a) Free energy diagram for pristine $Hf_2NO_2$ (black line), $V_{Hf}$-$Hf_2NO_2$ (red line) and $V_N$-$Hf_2NO_2$ (blue line). Faded lines indicate non-preferred alternative pathways. (b) & (c) the deformation charge density of *COOH and *HCOOH on pristine $Hf_2NO_2$, respectively. The isosurface value plotted is 0.005 e/bohr$^3$ (0.034 e/Å$^3$). Charges flow out from blue areas into yellow areas. The charge migration of molecule (*HCOOH) is much smaller than molecular fragment (*COOH), which testifies the weaker interaction between molecule and substrate in the former case.

Among the different $M_2XO_2$ defective MXenes studied here, the best candidates are: $V_{Zr}$-$Zr_2NO_2$, $V_{Hf}$-$Hf_2NO_2$, $V_W$-$W_2NO_2$ and $V_N$-$Ta_2NO_2$ with very low $UL_{CO2}$ ranging from -0.28 to -0.35 V vs. RHE (Table 1, all other MXenes in Table S4). This translates to low theoretical overpotentials of 0.45 to 0.52 V, since the equilibrium potential for $CO_2$ reduction to $CH_4$ is 0.17 V vs. RHE.[1d] Therefore, we believe the introduction of vacancy can enhance some types of $M_2XO_2$ MXenes' catalytic activity.

**Table 1.** The most promising defective MXenes in this study.

| No. | MXenes | $UL_{CO2}$ (V) | Overpotential (V) |
|---|---|---|---|
| 1 | $V_{Zr}$-$Zr_2NO_2$ | -0.28 | 0.45 |
| 2 | $V_{Hf}$-$Hf_2NO_2$ | -0.28 | 0.45 |
| 3 | $V_W$-$W_2NO_2$ | -0.31 | 0.48 |
| 4 | $V_N$-$Ta_2NO_2$ | -0.35 | 0.52 |

## Scaling relationship

To see if the vacancies affect the scaling relation between similarly bound intermediates, we compare the binding energies of the –C coordinated fragment-type (Figure 3a) and the –H coordinated molecule-type intermediates (Figure 3b). It is clear that the presence of vacancy does not alter the linearity of the scaling relationship, suggesting that the slope of the volcano curve is not likely to be influenced. However, the dissimilar response of the intermediates towards the vacancies means that the overall $UL_{CO2}$ may still be altered. A possible optimisation mechanism can be found in the $UL_{CO2}$ contour map with respect to *$H_2CO$ (odd-step) and *COOH (even-step) binding energy (ZPE and entropy corrected, Figure 3c). The $UL_{CO2}$ appears to be much more profoundly influenced by the *COOH, as the *$H_2CO$ binding energy range is relatively narrow between -1.0 to -0.7 eV for most cases. The range for *COOH is much wider at -2.0 to +0.5 eV, and the least negative $UL_{CO2}$ (red contoured area) can be achieved around -0.7 to -0.3 eV *COOH binding energy range.

The narrow range of *$H_2CO$ binding energy suggests that it is relatively unchanged by either $V_M$

or $V_X$. Thus, the evolution of $Hf_2NO_2$ catalytic performance can be illustrated by taking a cross sectional view of the $UL_{CO2}$ contour map at *$H_2CO$ binding energy of -0.634 V. This value is the average of *$H_2CO$ binding energy in pristine $Hf_2NO_2$ (-0.665 eV), $V_{Hf}$-$Hf_2NO_2$ (-0.620 eV) and $V_N$-$Hf_2NO_2$ (-0.617 eV). As seen in Figure 3d, the addition of N vacancy to $Hf_2NO_2$ structure ($V_N$-$Hf_2NO_2$) weakens the *COOH binding energy, moving it down the volcano curve (blue arrow) towards more negative $UL_{CO2}$. Conversely, $V_{Hf}$-$Hf_2NO_2$ strengthens *COOH binding energy and less negative $UL_{CO2}$ (red arrow) can be achieved. The exact result of adding $V_M$ or $V_X$ varies across individual MXenes (Fig S2), but generally our finding demonstrates that MXenes' $CO_2$RR performance can be tuned effectively by introducing a suitable defect type.

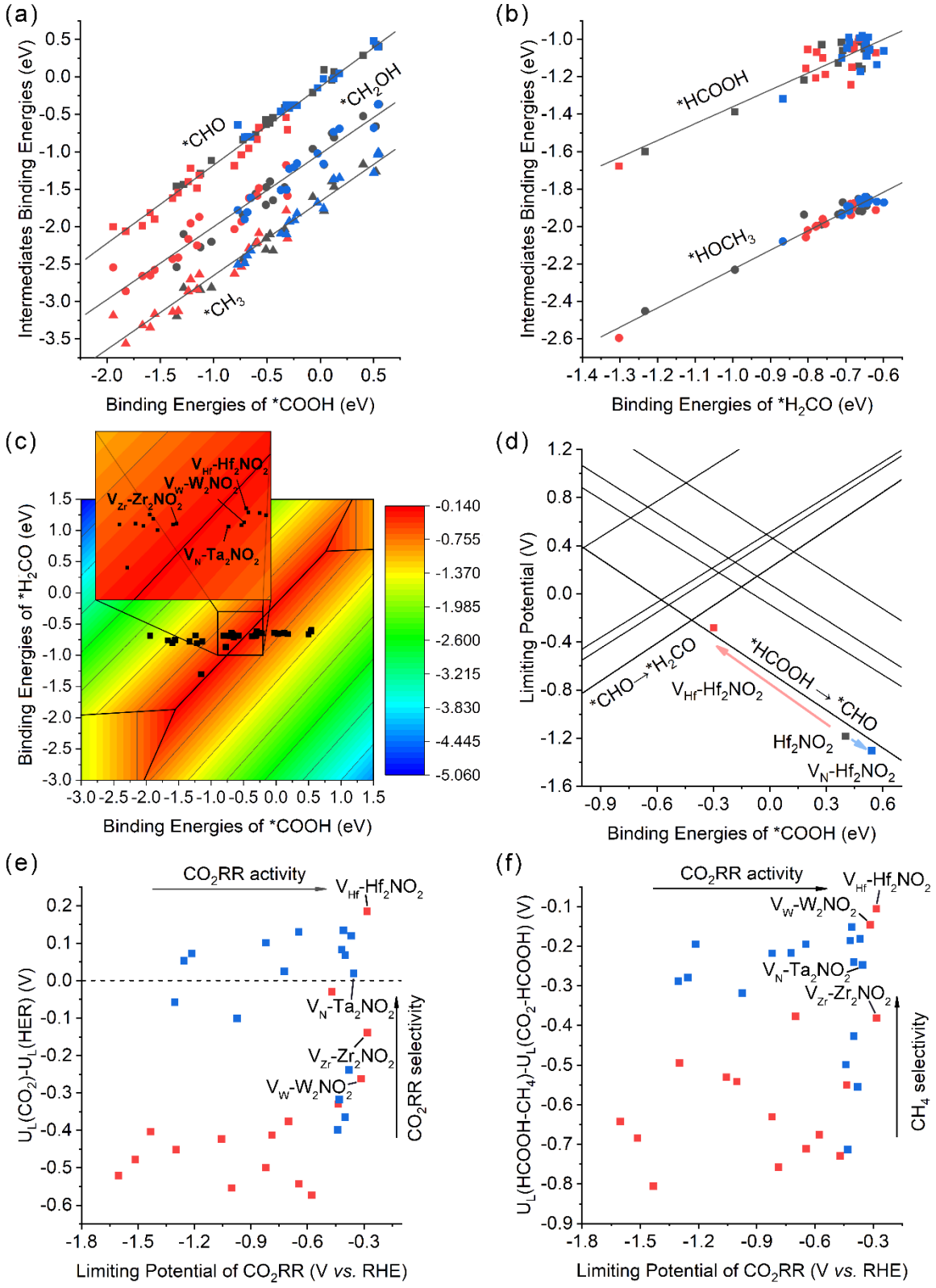


**Figure 3.** The scaling relations for (a) –C bound and (b) –H bound intermediates on $M_2XO_2$ MXenes. Purple, red and blue coloured data points represent pristine, $V_M$ containing and $V_X$ containing MXenes respectively. Different data point shapes represent different adsorbates. (c) A

$UL_{CO2}$ contour map as a function of *COOH and *$H_2CO$ binding energy. The catalysts located around the red contour (marked by a square and magnified) are predicted to have high $CO_2RR$ activity. (d) Cross-sectional view of the $UL_{CO2}$ contour map at *$H_2CO$ binding energy of -0.634 eV. (e) Relation between $UL_{CO2}$-$UL_{HER}$ and $UL_{CO2}$. $UL_{CO2}$-$UL_{HER}$ is used to indicate the $CO_2RR$ selectivity over HER. The more positive the value, the higher the $CO_2RR$ selectivity. (f). The relation between $UL_{(HCOOH-CH4)}$-$UL_{(CO2-HCOOH)}$ and $UL_{CO2}$. More positive $UL_{(HCOOH-CH4)}$-$UL_{(CO2-HCOOH)}$ indicates higher preference to form $CH_4$.

## Product distribution

HER is the most significant competing reaction during $CO_2RR$, especially in aqueous electrolytes, and it needs to be taken into consideration for MXenes as well.[16b, 22, 26] With an unpaired electron, *H is also a fragment-type intermediate that should also be significantly affected by $V_M$ or $V_X$. After calculating the *H binding energy (Table S6) and HER limiting potential ($UL_{HER}$),[27] the difference between $UL_{CO2}$ and $UL_{HER}$ can then be used to evaluate the selectivity for $CO_2RR$ *vs.* HER. It can be seen from Figure 3e that, while the majority of $M_2XO_2$ MXenes show preference towards HER ($UL_{CO2}$–$UL_{HER}$ < 0 V), 11 of them exhibit high selectivity towards $CO_2RR$. In particular, $V_{Hf}$-$Hf_2NO_2$ is identified to be the most promising catalyst with both high $CO_2RR$ activity and selectivity.

Along the pathway from $CO_2$ to $CH_4$, three kinds of molecule-type intermediates can be identified: formic acid (*HCOOH), formaldehyde (*$H_2CO$) and methanol (*$HOCH_3$). With weaker binding energy compared to fragment-type intermediates, these intermediates are also potential $CO_2RR$ products when desorbed from catalyst surface. The Faradaic yield of these molecules can be estimated by looking at the partial limiting potentials. Taking the case for $V_{Hf}$-$Hf_2NO_2$ (Fig 2a) as an example, the limiting potentials from *$H_2CO$ or *$HOCH_3$ to $CH_4$ ($UL_{H2CO-CH4}$ or $UL_{HOCH3-CH4}$) are positive, thus the Faradaic yield of these intermediates is predicted to be very small. However, the partial limiting potential from *HCOOH to $CH_4$ steps ($UL_{HCOOH-CH4}$) is negative (-0.28 V). Thus, comparatively it can

be said that HCOOH is a more likely product than $CH_4$ on $V_{Hf}$-$Hf_2NO_2$.

To get an indication of a more likely $CO_2$RR product distribution, the difference between the partial limiting potentials before *HCOOH intermediate ($UL_{HCOOH-CH4}$) and after ($UL_{CO2-HCOOH}$) can be obtained. Data compilation shown in Figure 3f shows negative ($UL_{HCOOH-CH4}$–$UL_{CO2-HCOOH}$) values for all $M_2XO_2$ MXenes, pristine or defective, indicating that the formation of HCOOH is generally more likely than $CH_4$. Nevertheless, $V_{Hf}$-$Hf_2NO_2$ displays the least negative ($UL_{HCOOH-CH4}$–$UL_{CO2-HCOOH}$) and $UL_{CO2}$ values, suggesting that it has the highest $CO_2$RR activity and $CH_4$ selectivity among $M_2XO_2$ MXenes studied here.

Considering that the *HCOOH→*CHO step (potential limiting for $CH_4$) and the $CO_2$→*COOH step (potential limiting for HCOOH) are parallel in the volcano curve (Fig 3d), radically different $UL_{HCOOH-CH4}$–$UL_{CO2-HCOOH}$ values are not expected in defective structures compared to the pristine counterpart. However, changes in $CO_2$RR product distribution may still occur (Table S5), due to the imperfect linear relationship and the altered *$H_2CO$ binding energy.

## Electronic structure

Thus far we have shown from the binding energy and $UL_{CO2}$ trends from appropriate types of vacancies can govern MXenes' catalytic $CO_2$RR performance. In order to uncover the intrinsic mechanism on how these vacancies affect the binding energy, we take a deeper look into the localised band structure.

First, we calculate the shift of Fermi level of the adsorbate system by setting the potential at the center of the vacuum as reference level (*i.e.* a shift in the work function). This way, the reference potential deviation caused by the additional defect states can be avoided.[28] Since we observe a linear relationship on all fragment-type intermediates (Figure 3a), it is thus acceptable to choose one of them

as a representative. Herein, we select *$CH_3$, the simplest of the fragment-type intermediates, to be a model to investigate the C-O chemical bond property. Next we investigate the relation between the change in the Fermi energy level ($\Delta E_{Fermi}$) upon vacancies creation with respect to the *$CH_3$ binding energy change ($\Delta E_{Binding}^{*CH_3}$). Interestingly, $\Delta E_{Fermi}$ appear to be linearly correlated with $\Delta E_{Binding}^{*CH_3}$ (Figure 4d, data and vacuum reference level correction in Table S7-S9). This means, $\Delta E_{Fermi}$ has the potential to be a simple descriptor in predicting the kind of defect that can result in a more positive $UL_{CO2}$.

We further calculate the local density of state (LDOS) between the O of the $Mo_2CO_2$ substrate and C of the *$CH_3$ adsorbate, and analysed the crystal orbital Hamiltonian population (COHP) of the C-O bond. The atomic configuration and bonds investigated are illustrated in Figure 4e. LDOS and COHP of $Mo_2CO_2$ shows clear binding energy difference between the pristine, $V_M$ and $V_X$ variants (Fig S2). The highly overlapping distribution of the LDOS of the substrate O and adsorbate C indicates that the orbitals are strongly hybridized (Figure 4a-c), corroborating that they form covalent bond. The anti-bonding state is only partially filled in this case, thus the occupancy ratio can be used as the gauge of the binding strength and reaction activity. Scarcely occupied anti-bonding states indicates strong bonding, which may inhibit reaction progression by suppressing the formation of the next adsorbate, while higher anti-bonding occupancy is likely to indicate weaker adsorption conversely.

In an attempt to correlate the density of state (DOS) and Fermi level change due to defects creation, we calculate three characteristic factors: (1) the division energy ($E_d$) between the bonding and anti-bonding states, (2) the bonding states centre ($E_{BC}$), and (3) the anti-bonding states centre ($E_{ABC}$). These three factors can be found in Figure 4(a-c). The state centres are calculated by:

$$E_{BC} = \frac{\int_{-\infty}^{E_d} E \times COHP \, dE}{\int_{-\infty}^{E_d} COHP \, dE}$$

$$E_{ABC} = \frac{\int_{E_d}^{0} E \times COHP \, dE}{\int_{E_d}^{0} COHP \, dE}$$

It can be clearly seen that as $V_M$ is introduced, the Fermi level is lowered and all 3 parameters ($E_d$, $E_{BC}$ and $E_{ABC}$) is brought closer to the Fermi level. On the contrary, the introduction of $V_X$ shifts these parameters away from the Fermi level.[29] Here, we propose to use the integrated COHP (ICOHP) to quantify the variation in the anti-bonding state occupation and reflect the bond strength (more negative ICOHP indicate stronger bonding).[27] ICOHP can be obtained by calculating the energy integral up to the highest occupied bands:[30]

$$ICOHP = \int_{-\infty}^{E_{Fermi}} COHP(E) \, dE$$

According to the ICOHP values listed in Figure 4(a-c), the introduction of $V_M$ induces more negative ICOHP value compared to the pristine $M_2XO_2$ case, while the presence of $V_X$ results in the opposite. This means that the ICOHP trend is in line with the binding energies of the fragment-type intermediates (Figure 3d), and the specific ICOHP values reflect the vacancy effect towards the electronic structure.

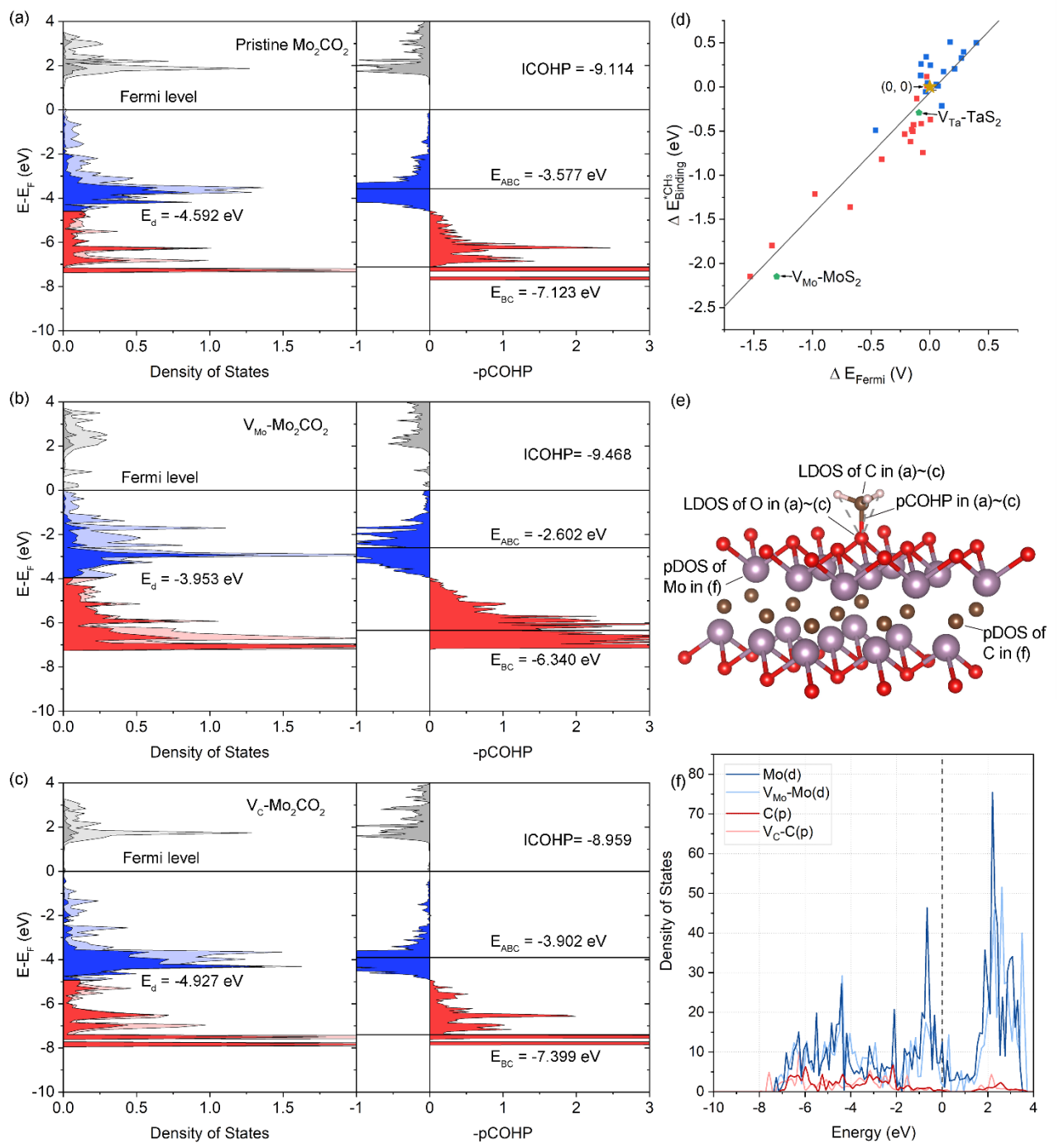


**Figure 4.** LDOS and pCOHP for *$CH_3$ on (a) pristine $Mo_2CO_2$, (b) $V_{Mo}$-$Mo_2CO_2$ and (c) $V_C$-$Mo_2CO_2$. The red, blue and grey colours represent the bonding anti-bonding and empty sates respectively. The lighter colours in the DOS diagram represent O atoms ($Mo_2CO_2$ substate) states, while bolder colours represent C atoms (*$CH_3$ adsorbate) states. The pCOHP are drawn as –pCOHP such that the bonding states are positive (to the right of x axis). (d) The relationship between the change of the Fermi level and change of *$CH_3$ binding energy. Red points represent $V_M$-$M_2XO_2$ while blue represent $V_X$-$M_2XO_2$. (e) The schematic of *$CH_3$ adsorbed on $Mo_2CO_2$ used in the DOS calculation. (f) The Mo and C pDOS of pristine and defective $Mo_2CO_2$ substrate. The 2p band of C is almost full, while d band of Mo is less filled.

Further, we propose that the shift in Fermi energy ($\Delta E_{Fermi}$) can be estimated by a simple formula:[31] (more details on the derivatisation of this formula can be referred to in SI section 7)

$$\Delta E_{Fermi} = \frac{\int_{-\infty}^{E_{F0}} \left(N d_0(E) - D(E)\right) dE - \delta}{D(E_{F0})}$$

Where $d_0(E)$ is the DOS (as a function of $E$) per formula unit for pristine $M_2XO_2$, $D(E)$ is the DOS for a supercell with $N$ formula units containing one vacancy, $D(E_{F0})$ is the DOS at the Fermi level, and $\delta$ represents the number of electrons that a neutral vacancy atom contains. It can be seen that the shift of Fermi level then depends on the difference between the change of the DOS upon vacancy addition ($\int_{-\infty}^{E_{F0}} \left(N d_0(E) - D(E)\right) dE$) and the change of the number of valence electrons ($\delta$). The change of states is sensitive to the filling rate of the band, since it is an integration up to $E_{Fermi}$, while the change of number of electrons only depends on the (atomic) type of the vacancy. In the case of $V_C$, $\delta$ is equal to 2 (ignoring any deep-lying orbitals). This means $\Delta E_{Fermi}$ can be quickly estimated to assess if a certain point defects will strengthen or weaken the binding of fragment-type intermediates ($\Delta E_{Binding}^{*fragment}$) and the corresponding $UL_{CO2}$.

To clarify why $V_M$ and $V_X$ exert opposite impact on the binding strength of fragment-type intermediates, the projected DOS (pDOS) of C and Mo in $Mo_2CO_2$ are calculated (Figure 4f). It can be seen that the C 2p bands are almost full, and the change in the DOS will be large when $V_X$ is introduced (the $\int_{-\infty}^{E_{F0}} \left(N d_0(E) - D(E)\right) dE = 6$ and $\Delta E_{Fermi} = (6 - \delta)/D(E_{F0})$, when $V_X$ is created from a completely full 2p band), making the $\Delta E_{Fermi}$ values likely to be positive. The situation for the Mo d band is different. Since most of the Mo *d* bands are above the Fermi level, the introduction of $V_M$ does not change the DOS significantly below the Fermi level (the $\int_{-\infty}^{E_{F0}} \left(N d_0(E) - D(E)\right) dE = 0$

and $\Delta E_{Fermi} = -\delta/D(E_{F0})$, when $V_M$ is introduced on a completely empty d band). This is reflected in Figure 4(d), where the points representing $V_M$-$M_2XO_2$ (red) are mostly located around $\Delta E_{Fermi} \approx 0$ and towards the bottom left corner, while the points representing $V_X$-$M_2XO_2$ (blue) are concentrated around the upper right corner.

Finally, we also find that the relationship between $\Delta E_{Fermi}$ and $\Delta E_{Binding}^{*CH_3}$ is extensible to other layered 2D catalysts such as $MoS_2$ and $TaS_2$ (Figure 4d, green pentagons). Similar to $V_M$-MXenes, $V_{Mo}$-$MoS_2$ and $V_{Ta}$-$TaS_2$ have more negative $\Delta E_{Fermi}$ and $\Delta E_{Binding}^{*CH_3}$ values (data and vacuum reference level correction in Table S10). Remarkably, the relationship between $\Delta E_{Fermi}$ and $\Delta E_{Binding}^{*CH_3}$ on these non-MXenes samples still fits the earlier prediction, indicating that $\Delta E_{Fermi}$ can be used to predict catalytic activity change on many other catalysts.

Based on our extensive analyses above, it can be clearly seen that the vacancy effect stems from the change in substrate-adsorbate interaction and electronic structure – both of which can be evaluated by the shift of Fermi level upon vacancy creation. More importantly, such an evaluation strategy using Fermi level change is also applicable to other catalysts, and possibly to other catalytic reactions beyond $CO_2$RR, enhancing the high throughput screening efforts for accelerated catalyst discovery.

# Conclusions

Through systematic investigation of defective $M_2XO_2$ type MXenes, we discover an effective strategy in lowering the overall $UL_{CO2}$ by exploiting the dissimilar response of fragment- and molecule-type intermediates towards M and X vacancies. The $UL_{CO2}$ tuning stems from the change in MXene electronic structure and the related substrate-adsorbate interaction upon vacancies creation. The most promising defective MXenes identified here is $Hf_2NO_2$ containing Hf vacancy, with a calculated $UL_{CO2}$

value of -0.28 V, which translates to a low overpotential of 0.45 V. A deeper look into the band structure reveals that vacancy creation also shifts the Fermi level linearly to the change in the adsorption strength of fragment-type intermediates ($\Delta E_{Binding}^{*fragment}$). This means that $\Delta E_{Fermi}$ can be used as a simple yet promising descriptor to gauge the overall impact of defects on the catalytic activity. More importantly, we also demonstrated that the linearity of $\Delta E_{Fermi}$-$\Delta E_{Binding}^{*fragment}$ is extensible to other catalyst systems beyond MXenes. As $\Delta E_{Fermi}$ can be estimated from the DOS, the linearity can potentially be exploited to hasten the screening and discovery of low-cost, eco-friendly, and high-performance materials based on a wide range of defective catalysts. Overall, our work established a bridge between the electronic structure and catalytic activity. We believe the fundamental understanding of the nature of defects will facilitate the development of $CO_2$RR and other multi-electron electrocatalytic reactions in the future.

# Experimental Section

## DFT calculation

Density functional theory (DFT) based first-principle scheme was employed for all calculations using the Vienna *ab-initio* Simulation Package (VASP). The projector-augmented-wave (PAW) pseudopotential was utilized to treat the core electrons. The revised Perdew-Burker-Ernzehof (RPBE) was chosen to simulate the electron interactions, which is considered to be more accurate in simulating adsorbate system.[32] DFT-D3 formalism is also adapted in order to take the van der Waals force correction into account.[33] A cut-off energy of 500 eV was applied for all the computations. Geometry optimization process were fully carried out until the residual force on each atom was less than 0.03 eV $Å^{-1}$. The thickness of vacuum is larger than 20 Å to avoid the artificial interaction among the periodic

slabs. In order to model the Schottky defect in MXenes, we remove one M atom (or X atom) from a pristine 3×3×1 supercell, with a Monkhorst-Pack 3×3×1 *k*-point mesh sampled Brillouin zone.

### CHE model

Computational hydrogen electrode (CHE) was applied to simulate the free energy diagrams and $UL_{CO2}$, where the free energy of proton-electron pair equals half the value of the $H_2$ at 0 V, at all pH values, at all temperature and at 101,325 Pa pressure. The change of free energy can be achieved by the following equation:

$$\Delta G = \Delta E_{elec} + \Delta E_{ZPE} - T \times \Delta S$$

where $\Delta E_{elec}$ is the electronic energy difference between two continuous steps, $\Delta E_{ZPE}$ is the change of the zero-point energy, $T$ is the temperature which is assumed as 298.15 K, while $\Delta S$ is the change of the entropy. ZPE and entropy of adsorbates are calculated from vibrations, which is treated in the harmonic oscillator approximation by standard methods.[34] As for the gas-phase molecule, the thermal corrections of translations and rotations are also taken into account. The specific data and calculation details can be found in Table S2.

## Acknowledgments

Q.F.Z. was supported by National Key Research and Development Program of China (No. 2017YFB0702100), Beijing Natural Science Foundation (2192029) and Technology Foundation for Selected Overseas Chinese Scholar, Ministry of Human Resources and Social Security of China. Z.W.S. was supported by the Singapore National Research Foundation (NRF-NRFF2017-04). D. L. was

supported by the European Regional Development Fund in the IT4Innovations national supercomputing center - path to exascale project, project number CZ.02.1.01/0.0/0.0/16_013/0001791 within the Operational Programme Research, Development and Education and SGS No. SP2020/150.

## Conflict of interest

The authors declare no competing financial interest.

**Keywords:** $CO_2$ reduction reaction • MXenes, two-dimensional • materials • first-principle simulation • defect engineering

[1] a) Z. W. Seh, J. Kibsgaard, C. F. Dickens, I. Chorkendorff, J. K. Nørskov, T. F. Jaramillo, *Science* **2017**, *355*, eaad4998; b) M. T. Koper, *Nanoscale* **2011**, *3*, 2054-2073; c) S. N. Steinmann, C. Michel, R. Schwiedernoch, P. Sautet, *Phys. Chem. Chem. Phys.* **2015**, *17*, 13949-13963; d) A. D. Handoko, F. Wei, B. S. Yeo, Z. W. Seh, *Nat. Catal.* **2018**, *1*, 922-934.

[2] a) M. Liu, Y. Pang, B. Zhang, P. De Luna, O. Voznyy, J. Xu, X. Zheng, C. T. Dinh, F. Fan, C. Cao, F. P. G. d. Arquer, T. S. Safaei, A. Mepham, A. Klinkova, E. Kumacheva, T. Filleter, D. Sinton, S. O. Kelley, E. H. Sargent, *Nature* **2016**, *537*, 382; b) M.-J. Cheng, E. L. Clark, H. H. Pham, A. T. Bell, M. Head-Gordon, *ACS Catal.* **2016**, *6*, 7769-7777; c) D. D. Zhu, J. L. Liu, S. Z. Qiao, *Adv. Mater.* **2016**, *28*, 3423-3452.

[3] a) K. P. Kuhl, E. R. Cave, D. N. Abram, T. F. Jaramillo, *Energy Environ. Sci.* **2012**, *5*, 7050-7059; b) Y. Huang, A. D. Handoko, P. Hirunsit, B. S. Yeo, *ACS Catal.* **2017**, *7*, 1749-1756; c) A. D. Handoko, C. W. Ong, Y. Huang, Z. G. Lee, L. Lin, G. B. Panetti, B. S. Yeo, *J. Phys. Chem. C* **2016**, *120*, 20058-20067.

[4] S. Nitopi, E. Bertheussen, S. B. Scott, X. Liu, A. K. Engstfeld, S. Horch, B. Seger, I. E. L. Stephens, K. Chan, C. Hahn, J. K. Nørskov, T. F. Jaramillo, I. Chorkendorff, *Chem. Rev.* **2019**, *119*, 7610-7672.

[5] Z. Li, C. Ma, Y. Wen, Z. Wei, X. Xing, J. Chu, C. Yu, K. Wang, Z.-K. Wang, *Nano Res.* **2020**, *13*, 196-202.

[6] a) X. Zhang, Z. Zhang, J. Li, X. Zhao, D. Wu, Z. Zhou, *J. Mater. Chem. A* **2017**, *5*, 12899-12903; b) N. Li, X. Chen, W.-J. Ong, D. R. MacFarlane, X. Zhao, A. K. Cheetham, C. Sun, *ACS Nano* **2017**, *11*, 10825-10833; c) A. D. Handoko, K. H. Khoo, T. L. Tan, H. Jin, Z. W. Seh, *J.*

*Mater. Chem. A* **2018**, *6*, 21885-21890; d) H. Chen, A. D. Handoko, J. Xiao, X. Feng, Y. Fan, T. Wang, D. Legut, Z. W. Seh, Q. Zhang, *ACS Appl. Mater. Interfaces* **2019**, *11*, 36571-36579; e) A. D. Handoko, H. Chen, Y. Lum, Q. Zhang, B. Anasori, Z. W. Seh, *Iscience* **2020**, *23*, 101181.

[7] Z. Tian, C. Priest, L. Chen, *Advanced Theory and Simulations* **2018**, *1*, 1800004.

[8] X. Sang, Y. Xie, M.-W. Lin, M. Alhabeb, K. L. Van Aken, Y. Gogotsi, P. R. C. Kent, K. Xiao, R. R. Unocic, *ACS Nano* **2016**, *10*, 9193-9200.

[9] T. Hu, J. Yang, X. Wang, *Phys. Chem. Chem. Phys.* **2017**, *19*, 31773-31780.

[10] a) Y. Wang, P. Han, X. Lv, L. Zhang, G. Zheng, *Joule* **2018**, *2*, 2551-2582; b) R. Khaledialidusti, A. K. Mishra, A. Barnoush, *J. Mater. Chem. C* **2020**, *8*, 4771-4779; c) D. Zhao, Z. Chen, W. Yang, S. Liu, X. Zhang, Y. Yu, W.-C. Cheong, L. Zheng, F. Ren, G. Ying, *J. Am. Chem. Soc.* **2019**, *141*, 4086-4093; d) X. Zhao, X.-J. Zha, L.-S. Tang, J.-H. Pu, K. Ke, R.-Y. Bao, Z.-y. Liu, M.-B. Yang, W. Yang, *Nano Res.* **2020**, *13*, 255-264.

[11] a) Y. Jia, J. Chen, X. Yao, *Mater. Chem. Front.* **2018**, *2*, 1250-1268; b) Y. Jia, K. Jiang, H. Wang, X. Yao, *Chem* **2019**, *5*, 1371-1397; c) J. Kotakoski, A. Krasheninnikov, U. Kaiser, J. Meyer, *Phys. Rev. Lett.* **2011**, *106*, 105505; d) Z. Hou, X. Wang, T. Ikeda, K. Terakura, M. Oshima, M.-a. Kakimoto, *Phys. Rev. B* **2013**, *87*, 165401; e) S. Siahrostami, K. Jiang, M. Karamad, K. Chan, H. Wang, J. Nørskov, *ACS Sustain. Chem. Eng.* **2017**, *5*, 11080-11085.

[12] P. P. Sharma, J. Wu, R. M. Yadav, M. Liu, C. J. Wright, C. S. Tiwary, B. I. Yakobson, J. Lou, P. M. Ajayan, X. D. Zhou, *Angew. Chem. Int. Edit.* **2015**, *54*, 13701-13705.

[13] a) J. Wu, M. Liu, P. P. Sharma, R. M. Yadav, L. Ma, Y. Yang, X. Zou, X.-D. Zhou, R. Vajtai, B. I. Yakobson, *Nano Lett.* **2015**, *16*, 466-470; b) W. Li, M. Seredych, E. Rodríguez‐Castellón, T. J. Bandosz, *ChemSusChem* **2016**, *9*, 606-616.

[14] Y. Li, Q. Sun, *Adv. Energy Mater.* **2016**, *6*, 1600463.

[15] F. Calle-Vallejo, D. Loffreda, M. T. M. Koper, P. Sautet, *Nat. Chem.*, *7*, 403-410.

[16] a) L. Dai, Q. Qin, P. Wang, X. Zhao, C. Hu, P. Liu, R. Qin, M. Chen, D. Ou, C. Xu, *Sci. Adv.* **2017**, *3*, e1701069; b) P. Li, J. Zhu, A. D. Handoko, R. Zhang, H. Wang, D. Legut, X. Wen, Z. Fu, Z. W. Seh, Q. Zhang, *J. Mater. Chem. A* **2018**, *6*, 4271-4278; c) Y. Wang, Z. Chen, P. Han, Y. Du, Z. Gu, X. Xu, G. Zheng, *ACS Catal.* **2018**, *8*, 7113-7119.

[17] T. W. Hansen, A. T. DeLaRiva, S. R. Challa, A. K. Datye, *Acc. Chem. Res.* **2013**, *46*, 1720-1730.

[18] A. Enyashin, A. Ivanovskii, *J. Solid State Chem.* **2013**, *207*, 42-48.

[19] a) D. Magne, V. Mauchamp, S. Célérier, P. Chartier, T. Cabioc'h, *Phys. Chem. Chem. Phys.* **2016**, *18*, 30946-30953; b) R. Ibragimova, M. J. Puska, H.-P. Komsa, *ACS Nano* **2019**, *13*, 9171-9181.

[20] K. J. Harris, M. Bugnet, M. Naguib, M. W. Barsoum, G. R. Goward, *J. Phys. Chem. C* **2015**, *119*, 13713-13720.

[21] J. L. Hart, K. Hantanasirisakul, A. C. Lang, B. Anasori, D. Pinto, Y. Pivak, J. T. van Omme, S. J. May, Y. Gogotsi, M. L. Taheri, *Nat. Commun.* **2019**, *10*, 1-10.

[22] Z. W. Seh, K. D. Fredrickson, B. Anasori, J. Kibsgaard, A. L. Strickler, M. R. Lukatskaya, Y. Gogotsi, T. F. Jaramillo, A. Vojvodic, *ACS Energy Lett.* **2016**, *1*, 589-594.

[23] A. D. Handoko, S. N. Steinmann, Z. W. Seh, *Nanoscale Horiz.* **2019**, *4*, 809-827.

[24] A. El-Barbary, R. Telling, C. Ewels, M. Heggie, P. Briddon, *Phys. Rev. B* **2003**, *68*, 144107.

[25] L. G. M. Pettersson, A. Nilsson, *Top. Catal.* **2014**, *57*, 2-13.

[26] A. D. Handoko, K. D. Fredrickson, B. Anasori, K. W. Convey, L. R. Johnson, Y. Gogotsi, A. Vojvodic, Z. W. Seh, *ACS Appl. Energy Mater.* **2017**, *1*, 173-180.
[27] J. K. Nørskov, T. Bligaard, A. Logadottir, J. R. Kitchin, J. G. Chen, S. Pandelov, U. Stimming, *J. Electrochem. Soc.* **2005**, *152*, J23-J26.
[28] L. Yu, A. Ruzsinszky, J. Perdew, *Nano Lett.* **2016**, *16*, 2444-2449.
[29] B. Hammer, J. K. Norskov, *Nature* **1995**, *376*, 238.
[30] V. L. Deringer, A. L. Tchougréeff, R. Dronskowski, *J. Phys. Chem. A* **2011**, *115*, 5461-5466.
[31] A. Malashevich, S. Ismail-Beigi, *Phys. Rev. B* **2015**, *92*, 144102.
[32] B. Hammer, L. B. Hansen, J. K. Nørskov, *Phys. Rev. B* **1999**, *59*, 7413.
[33] a) S. Grimme, J. Antony, S. Ehrlich, H. Krieg, *J. Chem. Phys.* **2010**, *132*, 154104; b) S. Grimme, S. Ehrlich, L. Goerigk, *J. Comput. Chem.* **2011**, *32*, 1456-1465.
[34] C. J. Cramer, F. Bickelhaupt, *Angew. Chem. Int. Edit.* **2003**, *42*, 381-381.

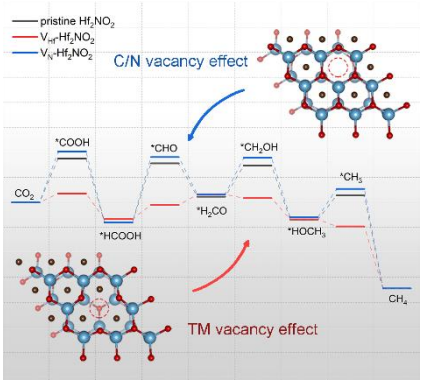


**Enhancing $CO_2$RR catalytic performance through vacancies:** Vacancies influence the binding energy of intermediates, and further affect the limiting potential of $CO_2$RR. The catalytic performance of MXenes can be enhanced by introducing a proper defect type. Furthermore, the shift of Fermi level can be a simple yet promising descriptor to predict the effect exerted by vacancies.